JAMES | Journal of Advances in Modeling Earth Systems®

ADVANCING EARTH AND SPACE SCIENCE

RESEARCH ARTICLE

10.1029/2021MS002759

Key Points:

- Cloud-resolving simulations of radiative-convective equilibrium exhibit a marked increase of anvil cloud fraction with resolution
- This sensitivity is closely related to the resolution-dependence of evaporation and precipitation efficiency
- The root of these sensitivities is the resolution-dependence of mixing between clear and cloudy air

Supporting Information:

Supporting Information may be found in the online version of this article.

Correspondence to:

N. Jeevanjee,
nadir.jeevanjee@noaa.gov

Citation:

Jeevanjee, N., & Zhou, L. (2022). On the resolution-dependence of anvil cloud fraction and precipitation efficiency in radiative-convective equilibrium. *Journal of Advances in Modeling Earth Systems*, *14*, e2021MS002759. https://doi.org/10.1029/2021MS002759

Received 10 AUG 2021
Accepted 3 FEB 2022

Author Contributions:

Conceptualization: Nadir Jeevanjee
Formal analysis: Nadir Jeevanjee
Methodology: Nadir Jeevanjee
Software: Nadir Jeevanjee, Linjiong Zhou
Validation: Linjiong Zhou
Visualization: Nadir Jeevanjee
Writing – original draft: Nadir Jeevanjee
Writing – review & editing: Linjiong Zhou

On the Resolution-Dependence of Anvil Cloud Fraction and Precipitation Efficiency in Radiative-Convective Equilibrium

Nadir Jeevanjee[1] and **Linjiong Zhou**[1]

[1]Geophysical Fluid Dynamics Laboratory, Princeton, NJ, USA

Abstract

Tropical anvil clouds are an important player in Earth's climate and climate sensitivity, but simulations of anvil clouds are uncertain. Here we identify and investigate one source of uncertainty by demonstrating a marked increase of anvil cloud fraction with resolution in cloud-resolving simulations of radiative-convective equilibrium. This increase in cloud fraction can be traced back to the resolution dependence of horizontal mixing between clear and cloudy air. A mixing timescale is diagnosed for each simulation using the cloud fraction theory of Seeley, Jeevanjee, Langhans, and Romps (2019) (https://doi.org/10.1029/2018GL080747) and is found to scale linearly with grid spacing, as expected from a simple scaling law. Thus mixing becomes more efficient with increasing resolution, generating more evaporation in middle and lower tropospheric updrafts. This decreases their precipitation efficiency (PE), thereby increasing their overall mass flux, leading to greater detrainment at the anvil level and hence higher anvil cloud fraction. The decrease in PE also yields a marked increase in relative humidity with resolution.

Plain Language Summary

High anvil-shaped clouds occurring in tropical thunderstorms are an important player in the climate system, but our understanding and simulations of this phenomena is uncertain. Here we show that the areal coverage of such “anvil” clouds in idealized simulations of the tropics is highly dependent on how finely the tropical atmosphere is represented in the simulation. Finer resolutions yield more evaporation and less rainfall per cloud, so then more clouds are required to provide the rainfall which the atmosphere requires, leading to an increase of cloudiness with resolution.

1. Introduction

Tropical anvil clouds exert considerable leverage over the Earth's radiation budget, by reflecting sunlight as well as trapping thermal infrared radiation (e.g., Hartmann et al., 2001). Any change in anvil cloud area with warming is thus a potentially significant climate feedback (Lindzen et al., 2001; Mauritsen & Stevens, 2015). Indeed, this “tropical anvil cloud area feedback” was recently assessed in the comprehensive review by Sherwood et al. (2020) to be -0.2 ± 0.2 W/m^2/K, a magnitude (and uncertainty) comparable to other cloud feedbacks, including low-cloud feedbacks.

While tropical anvil clouds and their area feedbacks are thus important players in the climate system, confidence in their simulation is low. Global climate models exhibit a significant spread in climatological anvil cloud fraction (Cesana & Chepfer, 2012; Su et al., 2013), as well as an uncertain sign in anvil cloud area feedbacks (Zelinka et al., 2016). Even limited-domain cloud-resolving models (CRMs) exhibit an uncertain sign in anvil cloud area changes with warming, with some CRMs exhibiting a decrease (Cronin & Wing, 2017; Romps, 2020) and others exhibiting an increase (Singh & O’Gorman, 2015). Similar ambiguities are found in global-scale, convection-permitting models (Narenpitak et al., 2017; Tsushima et al., 2014). Such uncertainty led Sherwood et al. (2020) to base their assessment of the anvil cloud area feedback almost entirely on observations (Williams & Pierrehumbert, 2017). This uncertainty in modeled anvil cloud area feedback is highlighted and reinforced by the results of the recent Radiative-Convective Equilibrium Model Intercomparison Project (Wing et al., 2020), which finds a strikingly large spread in both climatological anvil cloud fraction and anvil fraction changes with warming, across both convection-resolving and coarse-resolution simulations (see, e.g., their Figure 15).

Given the importance of anvil cloud area to climate, as well as the aforementioned uncertainties in their simulation, a deeper study of the fundamental physics of anvil clouds seems warranted. Although divergence and detrainment have long been recognized as key determinants of anvil cloud fraction (Hartmann & Larson, 2002), the recently developed formalism of Seeley, Jeevanjee, Langhans, and Romps (2019) (hereafter S19) emphasized the additional role of cloud lifetime in determining anvil cloud amount (see also Beydoun et al., 2021). While

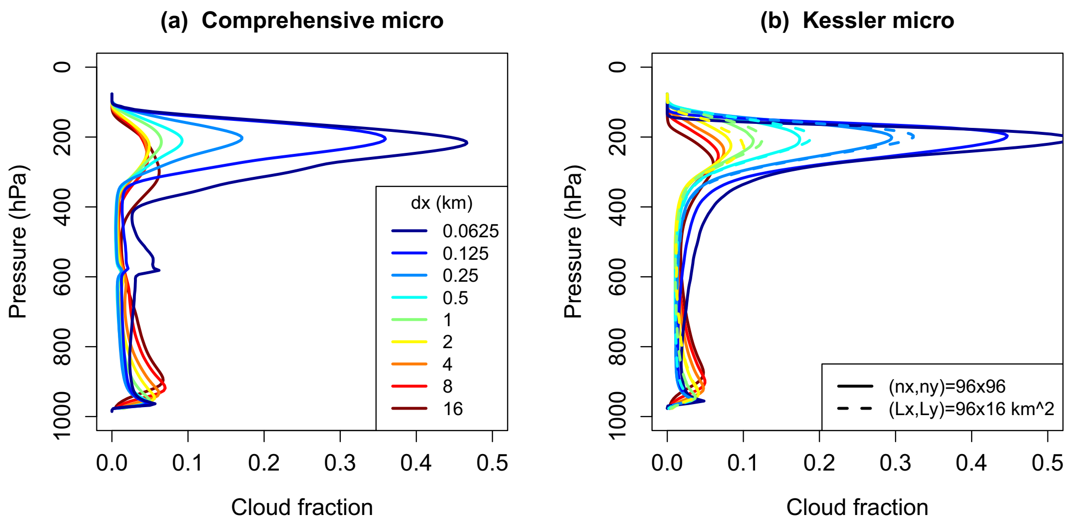

Figure 1. *A striking dependence of cloud fraction on resolution*. Time-mean cloud fraction profiles from Finite-Volume Cubed-Sphere Dynamical Core radiative-convective equilibrium simulations with varying horizontal resolution (colors). Left panel shows simulations with comprehensive microphysics, while the right panel shows simulations with simplified Kessler microphysics. All simulations are run on a 96×96 horizontal grid, except for those shown in dashed lines (right panel only) which were run on a fixed domain of size 96×16 km^2. Further simulation details are given in Section 2.

the lifetime of a cloudy parcel depends on a number of quantities, a key determinant in the S19 formalism is the characteristic timescale κ during which a volume of cloudy air mixes with an equal volume of clear air. This timescale influences a number of processes, including the rate of condensate evaporation, condensate dilution, and the spreading of anvil clouds.

The S19 formalism, and our physical picture of anvil cloud evolution in general, however, assumes that anvil clouds spread continuously after their detrainment from convective cores. But in simulations of cloud ensembles, such as cloud-resolving radiative-convective equilibrium (RCE), convective cores are typically only a few grid cells wide, even down to resolutions of O (100 m) (Jeevanjee, 2017). Thus, we might expect the spreading of anvil clouds in such simulations to be grid-dependent. Indeed, if the turbulent horizontal wind speed which advects air between grid cells is u_{rms}, then one expects the timescale κ (with which a cloudy grid cell completely mixes with a neighboring clear grid cell) to scale with horizontal grid spacing dx as

$$\kappa \sim dx/u_{\mathrm{rms}} \quad . \tag{1}$$

If this is true, and given the varied and significant influences of κ on cloud fraction, we might then also expect cloud fraction to depend on resolution. We confirm this in Figure 1 by plotting cloud fraction for a series of cloud-resolving RCE simulations with dx varying from 0.0625 to 16 km; details of these simulations are given in Section 2. The left panel shows simulations with the six-class GFDL microphysics scheme (Zhou et al., 2019), while the right panel shows simulations with a Kessler-type warm-rain microphysics scheme (Kessler, 1969, details below). The solid lines show simulations on a fixed grid, whereas dashed lines show simulations with a fixed domain size. A marked increase of high cloud fraction with increasing resolution is evident, and is found in all sets of simulations, suggesting that this result is robust. Similar results were also found when replacing our default modified PPM advection scheme (Lin, 2004) with a quasi-linear scheme with interior 2-Δ limiter, as well as when using an entirely different cloud-resolving model, DAM (Romps, 2008, see Figure S1 in Supporting Information S1).

This resolution-dependence adds to the aforementioned uncertainties in anvil cloud simulations, and casts further doubt on our ability to simulate anvil clouds with confidence. Furthermore, this decrease in confidence may have unfortunate implications for machine-learning applications in climate models, which sometimes use cloud-resolving simulations as “ground-truth” training data for AI algorithms (Brenowitz & Bretherton, 2018; Rasp et al., 2018; Yuval & O’Gorman, 2020). At the same time, however, a deeper understanding of this resolution sensitivity may lead to a better understanding of our simulations and of anvil cloud dynamics more generally, ideally pointing the way to more accurate simulations and parameterizations.

The goal of this paper is to pursue such understanding. Key components of this pursuit include not only the simulations shown in Figure 1, but also the theoretical framework of S19, as well as the process-level diagnostics required to utilize the theory. We begin in Section 2 by describing in detail our simulations and these process-level diagnostics. Section 3.1 then formulates a hypothesis for the resolution sensitivity seen in Figure 1, followed by a brief exposition of the S19 theory in Sections 3.2 and 3.3. Section 4 provides supporting evidence for the hypothesis of Section 3.1. We summarize and conclude in Section 5.

2. Simulations and Diagnostics

2.1. Simulations

The atmospheric model used here is the non-hydrostatic version of GFDL's FV^3 (Finite-Volume Cubed-Sphere Dynamical Core, Harris & Lin, 2013; Lin, 2004). The simulations analyzed here are very similar, and in some instances the same as, those performed in Jeevanjee (2017) (hereafter J17). We give the salient features of our simulations below and refer the reader to J17 for further details, as well as plots and animations depicting the character of the convection in these simulations.

As in J17, a guiding principle in configuring the simulations is to avoid inessential complexity insofar as possible (Jeevanjee et al., 2017). Thus, we run simple doubly periodic RCE simulations over a fixed sea surface temperature of 300 K, at resolutions spanning $dx = 0.0625 - 16$ km by factors of two. Radiative cooling is non-interactive and is parameterized as a fit to the invariant divergence of radiative flux F found by Jeevanjee and Romps (2018):

$$-\partial_T F = \left(0.025 \ \ \mathrm{W/m^2/K^2}\right) \cdot \left(T - T_{\mathrm{tp}}\right) \ . \tag{2}$$

Here the temperature derivative is a vertical derivative, $T_{\mathrm{tp}} = 200$ K is the tropopause temperature, and the above cooling is applied between the surface and 125 hPa, above which temperatures are relaxed to T_{tp} over a timescale of 5 days (so the stratosphere is roughly isothermal). The advantage of this non-interactive radiative cooling is that it is unaffected by the large changes in cloud fraction across our simulations, simplifying their analysis and interpretation. At the same time, cloud-radiation interactions are known to influence anvil and particularly anvil cirrus cloud development (e.g., Hartmann et al., 2018), so future work should investigate how such physics interacts with the mechanisms studied here. A first step in this direction is taken in the SI, where it is shown (using DAM, Figure S1 in Supporting Information S1) that cloud radiative effects do not materially affect the resolution-dependence of anvil cloud fraction.

No boundary layer or sub-grid turbulence schemes are used, though small amounts of vorticity and divergence damping are used to stabilize the model and reduce noise (see FV^3 documentation at https://repository.library.noaa.gov/view/noaa/30725). The "physics" time-step (at which the radiative cooling, surface flux, and microphysical parameterizations are called) ranges from 32 s at $dx = 16$ km to 2 s at $dx = 0.0625$ km, whereas the "acoustic" time-step (at which the prognostic fields are evolved by the fully compressible dynamical core) ranges from 16 s at $dx = 16$ km to 0.0625 s at $dx = 0.0625$ km. The vertical discretization is Lagrangian (Lin, 2004) with 151 levels, close to the values required for convergence in Ohno et al. (2019). The horizontal grid has 96 points in both x and y, except for the runs shown in dashed lines in Figure 1. These latter runs were more expensive, fixed-domain runs which due to computational constraints had a rectangular domain of 96×16 km^2 and were necessarily run over a smaller resolution range of $dx = 0.25 - 2$ km. These runs are further analyzed in the SI, where they are seen to behave very similarly to our fixed-grid runs.

Again in the spirit of avoiding inessential complexity, and to enable use of the theory of S19, microphysical transformations are performed with a warm-rain version of the GFDL microphysics scheme (Chen & Lin, 2013) which models only water vapor q_{v} (kg/kg), cloud condensate q_{c} (kg/kg), and rain, with the only transformations being condensation/evaporation of condensate (via saturation adjustment), rain evaporation, and autoconversion of cloud condensate to rain as

$$\left.\frac{dq_{\mathrm{c}}}{dt}\right|_{\mathrm{auto}} = -q_{\mathrm{c}}/t_{\mathrm{aut}} \tag{3}$$

where the autoconversion timescale $t_{\mathrm{aut}} = 30$ min. The only exceptions to this are the simulations shown in Figure 1a, which use the full complexity (six-class) GFDL microphysics scheme which includes ice processes (Zhou et al., 2019). While Equation 3 is extremely idealized, its use seems permissible since comprehensive microphysical processes do not seem essential for understanding how cloud fraction depends on resolution, mixing, and evaporation by saturation adjustment; indeed, this dependence is very similar for both our warm-rain and full complexity simulations (Figure 1).

2.2. Diagnostics

To analyze convection in our simulations we partition the domain online at each time step into active, inactive, and environmental air. Active (updraft) air has $q_c > q_{c0} \equiv 10^{-5}$ and vertical velocity $w > w_0$, where w_0 is resolution-dependent (consistent with the findings of J17) and varies between 0.25 and 1 m/s as documented in the SI (values for w_0 were chose by inspection of cloudy grid cells in simulation snapshots, and appropriate values will differ between models and model configurations). Inactive air has $q_c > q_{c0} = 10^{-5}$ and $w < w_0$ and should be thought of as detrained cloud. All other grid points are considered environmental. Cloud fraction C is diagnosed as the fractional area at a given height occupied by active and inactive air. We use this partitioning to conditionally average various quantities (w, q_c, etc.) over these subdomains. We also include microphysical diagnostics of condensate evaporation e (which does not include rain evaporation), autoconversion a, and condensation c (units kg/m^3/sec), all of which can also be conditionally averaged as above.

These primary diagnostics, while of interest in their own right, also allow us to derive other diagnostics of interest. One such diagnostic is the convective mass flux $M \equiv \rho w_{\mathrm{up}} \sigma_{\mathrm{up}}$ (kg/m^2/sec) where σ_{up} is the fractional area occupied by active updraft air at a given height, and the subscripts "up" and "in" refer to quantities which are conditionally averaged over active updrafts or inactive air, respectively. Another such diagnostic is the volumetric detrainment $\delta M/\rho$ (1/sec), where ρ is density and δ is fractional gross detrainment (fractional mass flux loss per unit height, units of 1/m, see De Rooy et al., 2013). The volumetric detrainment $\delta M/\rho$ can be interpreted as the fractional rate at which air at a given height becomes detrained cloud (i.e., inactive), and is diagnosed indirectly (following S19) by considering the cloud water budget for inactive air, which has detrained condensate $\delta M q_{\mathrm{c,up}}$ as the sole source term (no condensation) and total condensate evaporation and inactive autoconversion $e + a_{\mathrm{in}}$ as sinks (Condensate evaporation occurs in both inactive grid cells as well as the environmental grid cells adjacent to inactive ones, so we must use total e rather than e_{in}. Evaporation in active grid cells is negligible.) If we assume a steady-state, so that these condensate sources and sinks balance, we then have

$$\frac{\delta M}{\rho} = \frac{e + a_{\mathrm{in}}}{\rho q_{\mathrm{c,up}}} \ . \tag{4}$$

The right-hand side of this equation may be diagnosed from the simulations, yielding a method for diagnosing $\delta M/\rho$. Since M and ρ can also be diagnosed independently, this also yields a method for diagnosing the fractional detrainment δ. It should be noted that this indirect method of diagnosing detrainment relies critically on the steady-state assumption, which supplies the equality in Equation 4; without such an assumption one must directly diagnose detrainment, which is a more complicated endeavor (Dawe & Austin, 2010; Romps, 2010).

We initially spun up a $dx = 1$ km simulation for 200 days, and then branched all other runs off this run, running for at least 50 days to allow adjustment to different resolutions. All quantities analyzed in this paper are averaged horizontally and over the last 5 days of simulation.

3. Hypothesis and Theory

3.1. Hypothesis for Cloud Fraction Sensitivity

We now sketch a hypothetical explanation for the dramatic increase of cloud fraction with resolution seen in Figure 1. Later sections of the paper will buttress this initial explanation with further evidence.

Equation 1 implies more effective mixing at higher resolutions, hence greater evaporation. Greater evaporation suggests a decrease in the conversion efficiency $(c - e)/c$ (Lutsko & Cronin, 2018; Langhans et al., 2015), which is the fraction of condensate which turns to rain and is a vertically resolved measure of precipitation efficiency (PE). Since the non-interactive radiative cooling (2) fixes the amount of latent heating which convection must

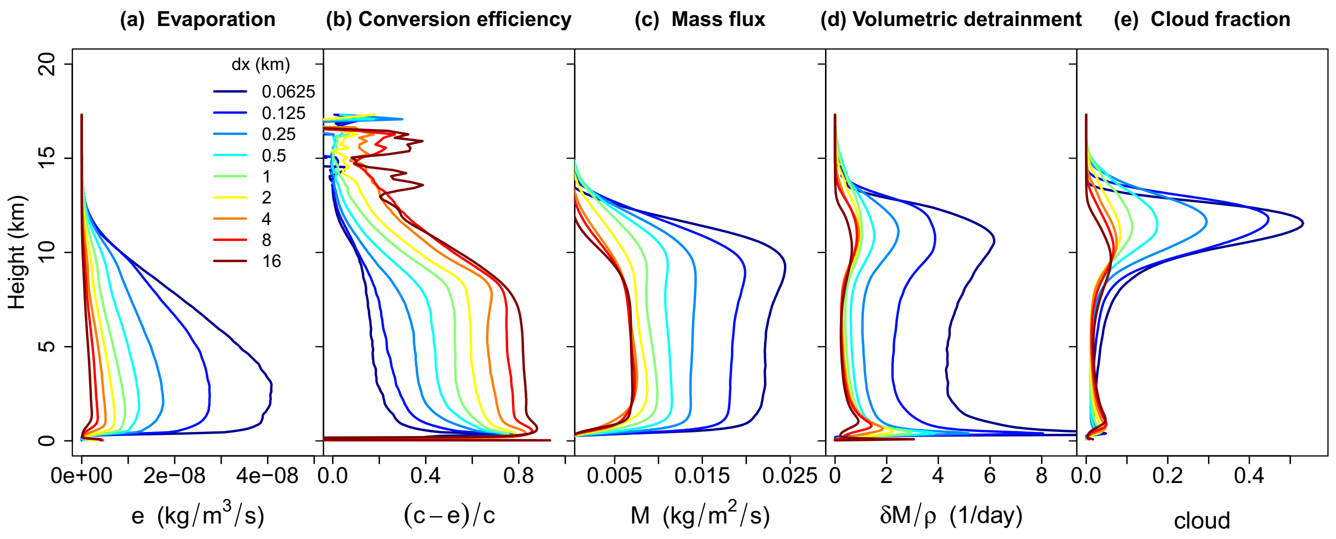

Figure 2. *Increasing evaporation with resolution leads to increased cloud fraction*. These panels show the quantities appearing in the the hypothesis 5, as a function of both height and resolution *dx*. A qualitative consistency between the simulations and the hypothesis 5 is evident. All quantities are diagnosed as described in the main text.

provide, a decrease in conversion efficiency implies that the convective mass flux must increase. But if mass fluxes go up, gross detrainment should too, leading to increased cloudiness. We summarize this hypothesis as

$$\begin{array}{l}\text{Increased}\\\text{evaporation}\end{array} \rightarrow \begin{array}{l}\text{Decreased}\\\text{PE}\end{array} \rightarrow \begin{array}{l}\text{Increased}\\\text{mass flux}\end{array} \rightarrow \begin{array}{l}\text{Increased}\\\text{detrainment}\end{array} \rightarrow \begin{array}{l}\text{Increased}\\\text{cloudiness}\end{array}. \tag{5}$$

Figure 2 shows that qualitatively, the above quantities (diagnosed as outlined in the previous section) behave as hypothesized. Note that the changes in evaporation with resolution occur predominantly in the mid and lower troposphere, rather than the anvil level (where saturation deficits are small and evaporation is ineffective, S19). So the mechanism outlined above is actually *non-local* in the vertical: Increased evaporation in the mid and lower troposphere reduces PE and increases mass flux, which then increases detrainment at the anvil level and hence anvil cloud fraction.

While this explanation is plausible, greater confidence in the hypothesis 5 requires quantitative confirmation of the proposed relationships, including the basic scaling 1. These tasks will be taken up in the next sections, and will be facilitated by the S19 theory, which we describe next.

3.2. Theory I: Cloud Fraction as Source Times Lifetime

To test the narrative in Equation 5 we will employ the cloud-fraction theory of S19. The theory consists of two major components. The first is a decomposition of cloud fraction C into a source times a lifetime, where the source is volumetric detrainment $\delta M/\rho$ and the lifetime τ_{cld} represents the time it takes for a detrained, cloudy parcel to cease being cloudy (i.e., $q_c < q_{c0}$). Following S19 we write this as

$$C = \frac{\delta M}{\rho}\tau_{\mathrm{cld}} \ . \tag{6}$$

Since C and $\delta M/\rho$ are readily diagnosed as described above, one can then diagnose τ_{cld} using 6; these quantities are plotted in Figure 3. A few features are worth noticing. The first is that in the mid-troposphere, τ_{cld} decreases markedly with resolution, which as discussed below is due to more efficient mixing and evaporation. In the upper troposphere, however, τ_{cld} only varies by a factor of two or so, and does so non-monotonically with *dx*. Thus, changes in upper-tropospheric τ_{cld} are not dominating the *dx*-dependence of cloud fraction there. From Equation 6 we can then conclude that the increase of anvil cloud fraction with resolution must instead be primarily due to increases in volumetric detrainment $\delta M/\rho$, as hypothesized in 5.

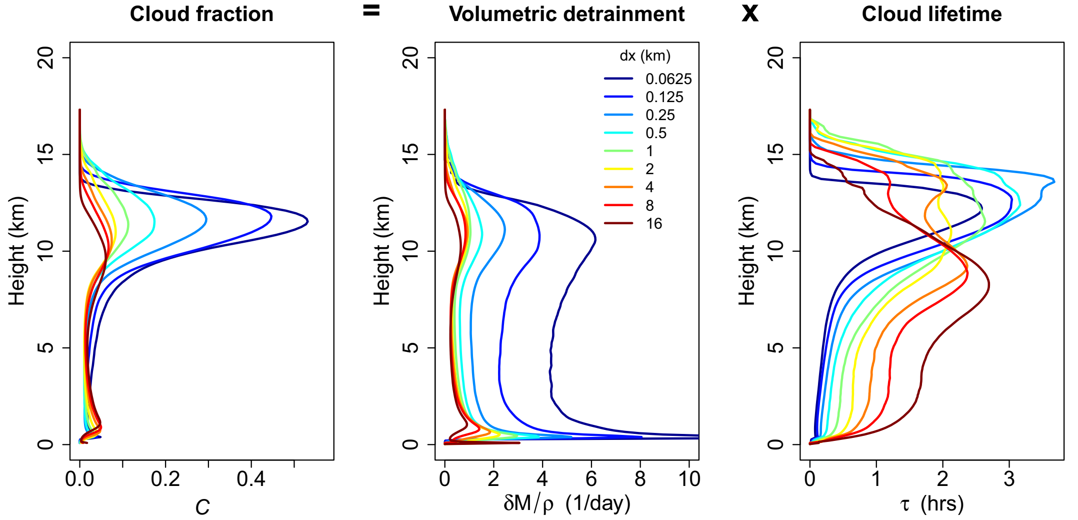

Figure 3. *Anvil cloud fraction changes are dominated by detrainment changes*. These panels show the quantities appearing in Equation 6, as a function of height and resolution. Since τ_{cld} at the anvil level does not exhibit a strong trend with resolution, the strong trend in anvil cloud fraction with resolution is due to the trend in volumetric detrainment $\delta M/\rho$.

3.3. Theory II: Analytical Model for Cloud Lifetime

The second component of the theory is an analytical model for the cloud lifetime τ_{cld}. Though we found above that changes in τ_{cld} at the anvil height do not directly drive anvil cloud fraction changes, we will see below that the changes in τ_{cld} in the lower and middle troposphere reflect the changes in mixing which do end up driving anvil cloud changes (as per the hypothesis 5). In fact, combining the analytical model for τ_{cld} with Equation 6 will allow us to diagnose mixing timescales κ for each of our simulations, allowing us to test Equation 1 which is a linchpin of our analysis.

The analytical model for τ_{cld} begins with an ordinary differential equation for cloud condensate q_{c} in a detrained parcel, assuming that evaporation and warm-rain autoconversion on a fixed timescale t_{aut} are the only sinks of cloud water:

$$\frac{dq_{\mathrm{c}}}{dt} = \underbrace{-\frac{1}{\kappa}\frac{1}{1+t/\kappa}\left[q_{\mathrm{c}} + (1-\mathrm{RH})q_{\mathrm{v}}^{*}\right]}_{\text{mixing}} - \underbrace{\frac{q_{\mathrm{c}}}{t_{\mathrm{aut}}}}_{\text{autoconversion}} . \tag{7}$$

The expression $q_{\mathrm{c}} + (1-\mathrm{RH})q_{\mathrm{v}}^{*}$ is the total water mass required to homogenize a unit mass of clear air that is mixed into the inactive cloudy air, while $1 + t/\kappa$ is the mass of the parcel at time t relative to its initial (unit) mass, and $1/\kappa$ is the mixing rate. For a complete derivation of Equation 7, see S19.

Equation 7 can be solved analytically, and an analytical formula for the lifetime τ_{cld} at which $q_{\mathrm{c}} < q_{\mathrm{c0}}$ can be derived (Equation A2). This formula contains κ as an undetermined parameter, to be determined by optimization. We optimize κ by minimizing the RMSE between the simulated cloud fraction and that given by Equation 6, where $\delta M/\rho$ is diagnosed directly from the simulations but τ_{cld} is given by Equation A2. The results of this optimization for each of our warm-rain (Kessler) simulations is shown in Figure 4. One can see that for $dx > 0.5$ km or so, the S19 theory captures the simulated cloud fraction profiles reasonably well. For $dx \lesssim 0.5$ km the fit degrades, likely due to our neglect of anvil cloud spreading (Appendix A.2). What is of interest here, however, are the values for κ diagnosed from each of these fits, which are noted in each panel in Figure 4 and also shown in Figure 5. Figure 5 also shows a linear fit of the form $\kappa = dx/u_{\mathrm{rms}}$. This figure shows that the scaling 1 is indeed consistent with our simulations and the S19 theory (which was used to diagnose κ). Furthermore, the u_{rms} value derived from the linear fit is 0.1 m/s, roughly consistent with the root-mean square horizontal velocities seen in our simulations (Figure S4 in Supporting Information S1).

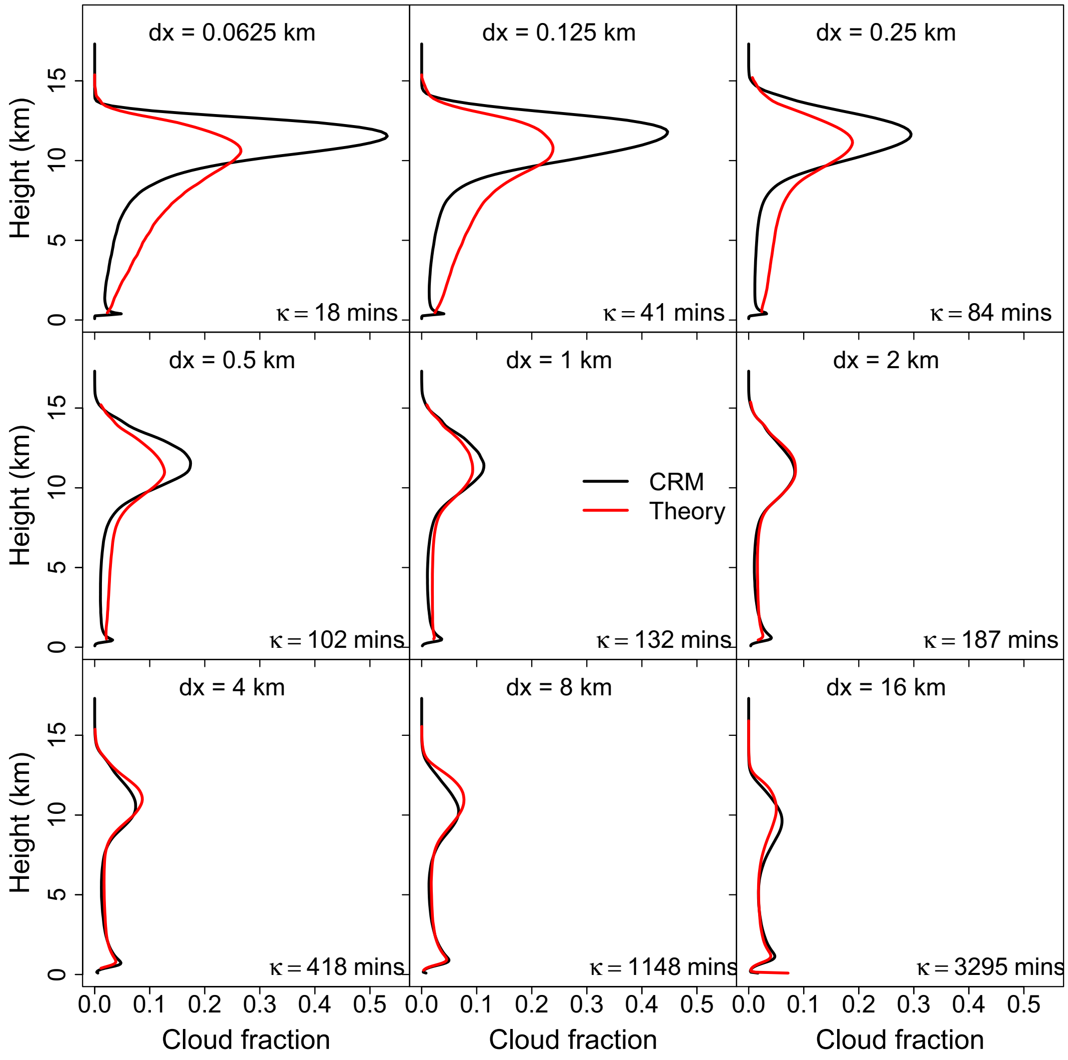

Figure 4. *The S19 theory approximates the simulated cloud fraction, and diagnoses a dx-dependent κ.* These panels show the simulated cloud fraction profile at a given resolution dx (black lines), along with the prediction from the S19 theory (red lines, Equation A2 and 6). The S19 theory approximates the simulated cloud fraction profiles reasonably well for $dx \gtrsim 0.5$ km. The S19 theory also yields, via optimization, a value for κ at each dx, noted in the lower right of each panel.

4. Evaporation, PE, and Mass Flux

The last section presented evidence that simulated mixing increases with resolution following 1. But, how do we know that this mixing is behind the changes in evaporation manifest in Figure 2a? And how do we know that these evaporation changes indeed cause the PE changes in Figure 2b, and that these PE changes indeed drive the mass flux changes seen in Figure 2c? We turn to these questions now.

To assess the influence of the mixing timescale κ on condensate evaporation, we note that by Equation 7 the evaporation rate in the neighborhood of an updraft grid cell (neglecting inactive grid cells whose contribution in the mid and lower troposphere is small) should just be ρ times the mixing term, which we evaluate at $t = 0$ for simplicity. This yields two contributions which can be read off from Equation 7, and which can be interpreted as follows. The $\rho\kappa^{-1}(1 - \mathrm{RH})q_v^*$ term represents condensate evaporation in the cloudy grid cell, which must occur to bring newly entrained environmental air to saturation. Then there is the $\rho\kappa^{-1}q_{\mathrm{c,up}}$ term, which represents the condensate which is advected into the clear grid cell and then subsequently evaporates. Averaging these terms over the domain yields a factor of σ_{up}, and invoking (1; again with $u_{\mathrm{rms}} = 0.1$ m/s) then yields finally

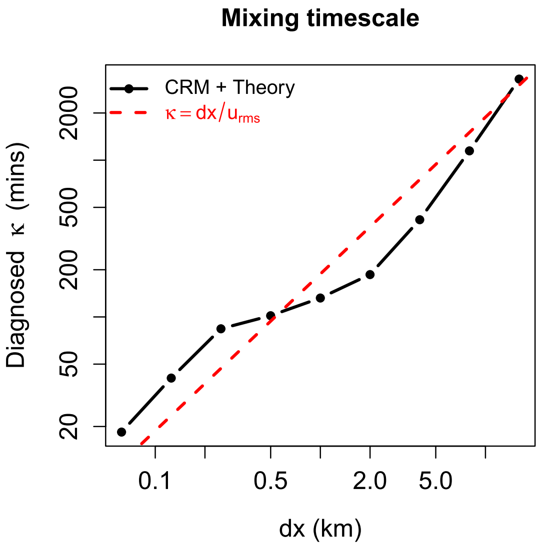

Figure 5. *Diagnosed mixing timescale κ depends linearly on resolution.* This figure shows the values of κ diagnosed as in Figure 4, as a function of dx (black dots and lines). Also shown is a linear fit of the form 1 with $u_{\rm rms} = 0.1$ m/s (red line). The reasonable agreement supports the linear scaling 1.

$$e = \frac{\rho u_{\rm rms}}{dx}\sigma_{\rm up}\left[q_{\rm c,up} + (1-{\rm RH})q_{\rm v}^*\right] . \tag{8}$$

We compare this estimate of evaporation to that diagnosed directly from our simulations in Figure 6. The agreement between Figures 6a and 6b is reasonable, suggesting that Equation 8 is indeed a good first-order description of the evaporation rate.

However, Equation 8 tells us that the evaporation rate e is proportional not only to $1/dx$, but also to the fractional updraft area $\sigma_{\rm up,}$ which itself also increases with resolution (since $M \sim \sigma_{\rm up}$, cf. Figure 2c). To confirm the central role of the dx-dependence in Equation 8, Figure 6c shows the evaporation rate e normalized by the mass flux M, which can be interpreted as the rate at which $q_{\rm c,up}$ decreases (due to evaporation) in a convecting parcel per unit height traveled. This quantity increases markedly with resolution, confirming that the proportionality between e and $1/dx$ in 8 is a primary influence on evaporation rates.

How do these marked increases in evaporation, even measured relative to mass flux M, relate to the actual increases in M? The hypothesis 5 posits that this increase in mass flux is due to a decrease in PE from enhanced mixing. To check this connection, we calculate PE as precipitation P (kg/m^2/s) divided by vertically integrated condensation, that is, PE $\equiv P/\int c dz$. We also calculate a vertically averaged $\langle M \rangle$ over 2 and 10 km (the range over which M in each simulation is roughly constant). Following Held and Soden (2006) we then argue that atmospheric energy balance dictates that the fixed column integrated radiative cooling $Q = 120$ W/m^2 should equal PE times an estimated cloud base moisture flux of $Lq_{\rm v,\,bl}\langle M \rangle$, where the boundary-layer humidity $q_{\rm v,\,bl} = 0.017$ kg/kg is calculated as the time-mean lowest-level humidity averaged across all the simulations (an implicit assumption here is that all of the cloud base moisture flux condenses somewhere in the free troposphere). Then $\langle M \rangle$ and PE should be related as

$$\langle M \rangle \approx \frac{Q}{Lq_{\rm v,\,bl}}\frac{1}{\rm PE} . \tag{9}$$

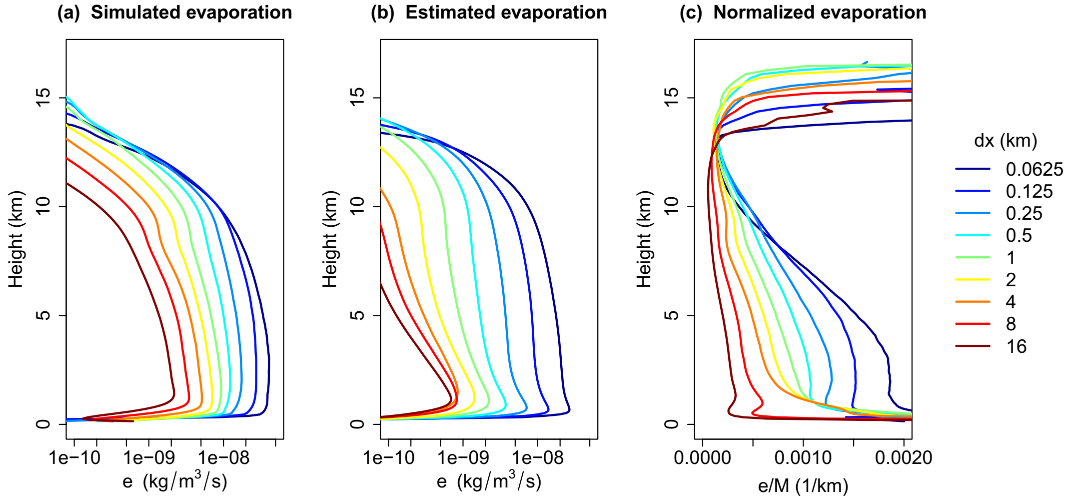

Figure 6. *Evaporation scales as* $1/dx$, *as captured by Equation* 8. The vertically resolved evaporation e diagnosed directly from our simulations (panel a) is well approximated by Equation 8 (panel b). Normalizing evaporation by the mass flux M (panel c) confirms that the $1/dx$ factor in Equation 8 is influencing evaporation rates. *Note* the logarithmic x-axis in panels a,b.

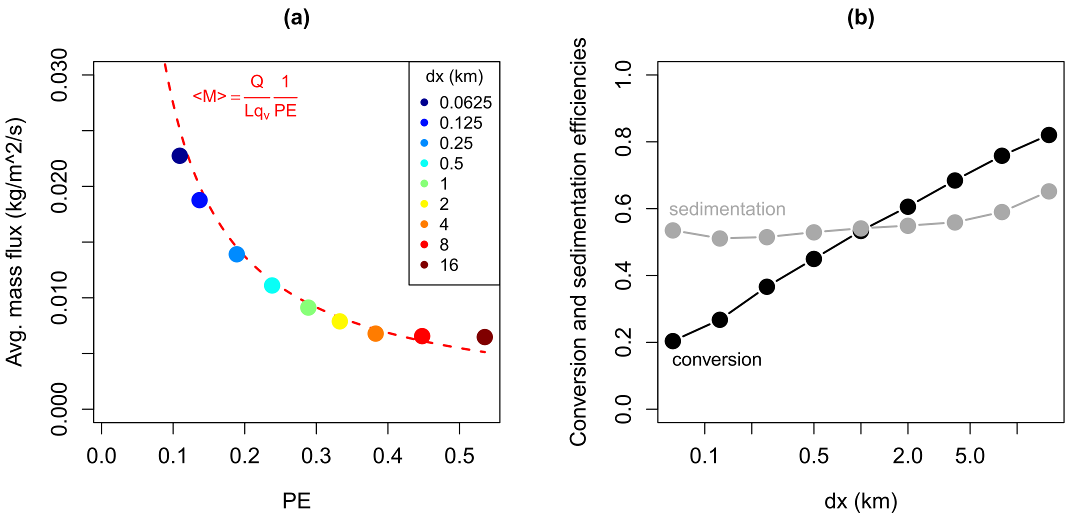

Figure 7. *Mass fluxes increase with decreasing PE, as dictated by energy balance*. Panel (a) shows vertically averaged mass-flux $\langle M \rangle$ plotted against precipitation efficiency, defined as precipitation divided by vertically integrated condensation, for our simulations at varying *dx* (colored points). Also shown is the relationship 9, which is an expression of atmospheric energy balance (red dashed line). A strong decrease of PE with *dx* is evident, and the mass flux covaries according to 9. Panel (b) shows that the PE changes with resolution are indeed due to changes in conversion efficiency, rather than sedimentation efficiency.

This relationship, along with $\langle M \rangle$ and PE calculated from the simulations, is shown in Figure 7a. This panel shows that PE indeed decreases markedly as resolution increases, and that the corresponding increase in mass flux is indeed consistent with atmospheric energy balance as dictated by Equation 9. This provides quantitative confirmation of parts of the mechanism proposed in Equation 5, namely that more efficient evaporation reduces PE and hence increases M as resolution increases.

It should be noted, however, that PE can be decomposed as a product of a vertically integrated conversion efficiency CE (similar in spirit to the vertically resolved conversion efficiency shown in Figure 2) and a sedimentation efficiency SE which measures the impact of rain evaporation on surface rain rate (Lutsko & Cronin, 2018; Langhans et al., 2015). This decomposition is given by

$$\mathrm{PE} \;=\; \underbrace{\frac{\int (c-e)\,dz}{\int c\,dz}}_{\mathrm{CE}}\;\underbrace{\frac{P}{\int (c-e)\,dz}}_{\mathrm{SE}}\,. \tag{10}$$

The mechanism of Equation 5 posits that the resolution-dependence of PE arises from a resolution dependence of CE rather than SE. Figure 7b shows CE and SE diagnosed from the the expressions in Equation 10, and confirms that indeed the PE changes seen here are primarily due to changes in conversion efficiency rather than sedimentation efficiency.

As a further aside, we also note that the increase in condensate evaporation and decrease in PE with resolution might also be expected to cause increases in relative humidity (RH). Indeed, such a relationship was explicitly formulated in Romps (2014). While such changes in RH are not directly relevant to the changes in cloud fraction which are the focus of this paper, they are straightforward to understand using the theory of Romps (2014) in conjunction with the diagnostics developed here. For completeness, this analysis is presented in Appendix B.

5. Summary and Discussion

We summarize our main results as follows:

1. Cloud-resolving simulations exhibit a marked increase of anvil cloud fraction with resolution (Figure 1)

2. This sensitivity can be traced to the resolution-dependence of evaporation and hence PE (Equation 5, Figures 2, 6 and 7)
3. The root of this sensitivity is that the mixing which causes evaporation scales linearly with resolution (Equation 1, Figure 5)

A key ingredient in this analysis was the theory of S19, which allowed us to diagnose values of the mixing timescale κ for each simulation and hence verify Equation 1.

As an aside, one may wonder how these results are consistent with the "clear-sky convergence" (CSC) paradigm for high cloud fraction (S19 and references therein), which says that convective detrainment is determined by horizontal mass convergence in clear skies, which itself is determined by well-constrained radiative cooling profiles and moist adiabatic lapse rates. For simulations at a single surface temperature and with non-interactive radiative cooling as we have here, the CSC paradigm thus predicts a fixed detrainment profile, contradicting the hypothesis 5 as well as the simulation results (Figure 2d). The resolution of this paradox is twofold: (a) the CSC paradigm only accounts for radiative cooling as a diabatic heat source, and neglects cooling from condensate evaporation, and (b) The anvil level is precisely the level where lapse rates begin transitioning from moist adiabatic values toward the much stabler values of the stratosphere, so anvil level lapse rates are in fact unconstrained and may vary even at a fixed surface temperature. Note that the actual CSC in our simulations indeed increases with resolution, consistent with the increasing cloud fraction (Figure C1); we merely emphasize that this increase cannot be predicted by changes in radiative cooling profiles or moist adiabatic thermodynamics. A more detailed discussion of these issues, as well as evidence from simulations, is given in Appendix C.

Looking forward, this work raises a number of questions and possible future research directions. Perhaps most obvious is the question of whether the results found here generalize to more realistic simulations. Do regional or global simulations at O (1–10 km) resolution with explicit or superparameterized convection (e.g., Khairoutdinov et al., 2005; Prein, 2015; Satoh et al., 2019; Stevens et al., 2019) exhibit a similar resolution-dependence of PE and cloud fraction? Some global CRMs do seem to exhibit an increase of cloud fraction with resolution (e.g., Miyakawa & Miura, 2019; Roh et al., 2021), but further investigation, including an analysis of PE and for more models, would be useful. Given the relevance of both anvil clouds and PE for weather and climate (Sui et al., 2020), such a resolution-dependence would raise questions about the fidelity and utility of convection-resolving global models, both as general-purpose "digital twins" of Earth (Bauer et al., 2021; Voosen, 2020) and more specifically as benchmarks for machine learning, as mentioned in the introduction.

There are also other aspects of the resolution dependence which remain unexplored. For instance, the increase in evaporation and decrease in PE with resolution might be expected to reduce rainfall rates on short space and time scales, as less of the water in a given convective updraft will be available for conversion to precipitation. This seems consistent with some meteorological studies, such as Bryan and Morrison (2012), but could be studied more systematically in both RCE simulations as well as transient simulations of meteorological events.

Another avenue for exploration is the influence of convective organization on the results presented here. Would the mechanism of Equation 5 operate similarly when convection is organized and all updrafts experience an environment moister than the domain mean? We make a very preliminary investigation of this in SI Section 5, where we explore a limited set of "self-aggregated" RCE simulations which also appear to exhibit an increase of cloud fraction with resolution. A much more comprehensive investigation is warranted, however.

Finally, it is worth commenting on why the resolution-dependence of cloudiness is somewhat unique relative to other resolution sensitivities. In some sense, a resolution sensitivity of cloudiness is unsurprising because most aspects of atmospheric simulation, including wind fields, thermodynamic variables, and moisture variables, are sensitive to resolution to some degree (e.g., Bryan et al., 2003; Pauluis & Garner, 2006). What is unique about cloud condensate, however − especially relative to other tracers − is that its sources and sinks are largely given by saturation adjustment, which is a threshold process and thus inherently nonlinear. This means that a change in mixing efficiency doesn't merely redistribute a conserved amount of condensate in space; because of saturation adjustment, mixing can actually dramatically change how much condensate there *is*. Given the importance of clouds and precipitation to both weather and climate simulations, further study of how resolution, numerics, and subgrid mixing schemes affect cloud condensate in particular seems warranted.

10.1029/2021MS002759

Appendix A: Further Details of the Cloud Lifetime Model

A1. Derivation of Cloud Lifetime

Equation 7 is a linear ordinary differential equation (ODE) and can be solved by the usual method of finding particular and homogenous solutions and taking their sum. The homogenous solution is obtained by zeroing out the $(1-\mathrm{RH})q_\mathrm{v}^*$ term in Equation 7, yielding a separable ODE which can be integrated directly to obtain the homogenous solution proportional to $e^{-t/t_\mathrm{aut}}(1+t/\kappa)^{-1}$. The particular solution is obtained via an ansatz proportional to $(1+t/\kappa)^{-1}$, yielding the particular solution $-t_\mathrm{aut}\kappa^{-1}(1-\mathrm{RH})q_\mathrm{v}^*(1+t/\kappa)^{-1}$. Summing the particular and homogenous solutions (where the latter has an undetermined coefficient of proportionality) and imposing the initial condition that the initial q_c value for the detrained parcel is simply the updraft value $[q_\mathrm{c}\,(t=0)=q_\mathrm{c,up}]$, one obtains (see also S19)

$$q_\mathrm{c}(t)=\frac{1}{1+t/\kappa}\left[q_\mathrm{c,up}e^{-t/t_\mathrm{aut}}-\frac{t_\mathrm{aut}}{\kappa}(1-\mathrm{RH})q_\mathrm{v}^*\left(1-e^{-t/t_\mathrm{aut}}\right)\right]\quad . \tag{A1}$$

The factor of $(1+t/\kappa)$ is just the volume at time t relative to the parcel's initial volume, and thus its appearance in the solution above represents the effect of dilution of condensate as the parcel's volume grows. The first term in brackets represents the decay of q_c due to the autoconversion sink, and the second term represents the effect of condensate evaporation into entrained, subsaturated environmental air.

With the solution A1 in hand it is straightforward, if slightly tedious, to solve for the time τ_cld at which $q_\mathrm{c}=q_\mathrm{c0}$. Employing the Lambert W function (which satisfies by definition $x=W(x)e^{W(x)}$) we eventually obtain

$$\tau_\mathrm{cld}=t_\mathrm{aut}\left[W\left(ae^{b}\right)-b\right] \tag{A2a}$$

where

$$a=\frac{\kappa}{t_\mathrm{aut}}\frac{q_\mathrm{c,up}}{q_\mathrm{c0}}+\frac{(1-\mathrm{RH})q_\mathrm{v}^*}{q_\mathrm{c0}} \tag{A2b}$$

$$b=\frac{\kappa}{t_\mathrm{aut}}+\frac{(1-\mathrm{RH})q_\mathrm{v}^*}{q_\mathrm{c0}} \tag{A2c}$$

A2. Accounting for Anvil Spread

Multiplying τ_cld derived above by the volumetric detrainment as in 6 gives a time-mean cloud fraction, but this assumes that the cloud area stays fixed during its lifetime. Inspection of coarse-resolution ($dx \gtrsim 0.5$ km or so) simulations shows that this is a reasonable assumption, but at higher resolutions the anvils begin to spread before disappearing. This potentially explains the theory-CRM mismatch at high resolutions in Figure 4, as well as the enhanced resolution-sensitivity at high resolution seen in Figure 1. S19 incorporated anvil spreading into their model by integrating the cloud area $A(t)=A_0\,(1+t/\kappa)$ over time to obtain an *effective* cloud lifetime $\tilde{\tau}_\mathrm{cld}$:

$$\int_0^{\tau_\mathrm{cld}}A_0(1+t/\kappa)=A_0\left(\tau_\mathrm{cld}+\frac{\tau_\mathrm{cld}^2}{2\kappa}\right)\equiv A_0\tilde{\tau}_\mathrm{cld} \tag{A3a}$$

$$\text{where}\quad \tilde{\tau}_\mathrm{cld}=\tau_\mathrm{cld}+\frac{\tau_\mathrm{cld}^2}{2\kappa}\quad . \tag{A3b}$$

10.1029/2021MS002759

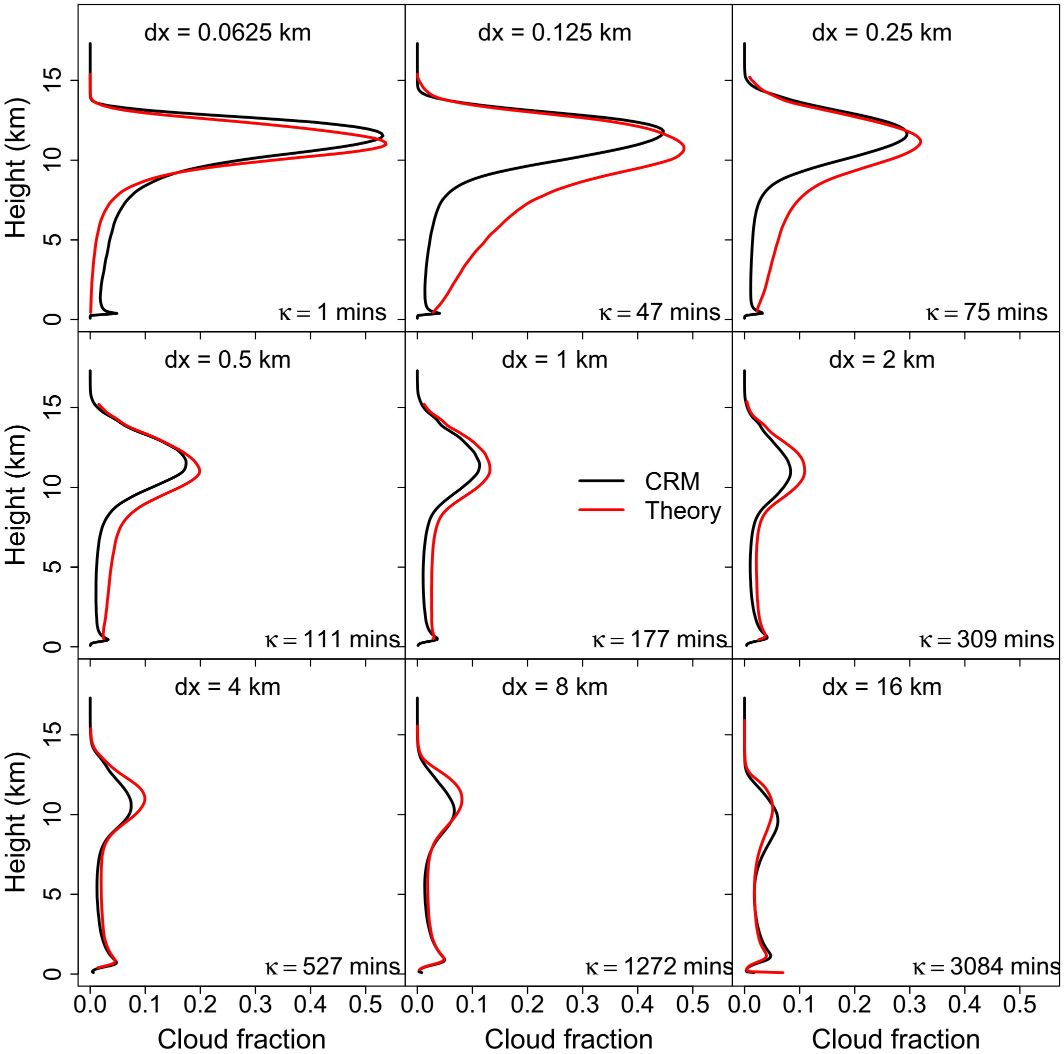

Figure A1. *Accounting for anvil spread improves predictions of anvil cloud fraction at high resolution, but degrades predictions of mid-tropospheric cloud fraction.* As in Figure 4, but using $\tilde{\tau}_{\text{cld}}$ from Equation A3b instead of τ_{cld} in Equation 6. Diagnosed κ values are similar to those in Figure 4, except for the $dx = 0.0625$ km case.

One then obtains an alternative theory for cloud fraction by substituting $\tilde{\tau}_{\text{cld}}$ for τ_{cld} in Equation 6. The predictions from this modified theory are shown in Figure A1. At coarser resolutions the modified cloud fraction profiles and associated κ values are quite similar to those in Figure A1. This is expected since at coarse resolutions $\kappa > \tau_{\text{cld}}$ ~150 min (at the anvil level, cf. Figure 3), so the additional term $\tau_{\text{cld}}^2/(2\kappa)$ in $\tilde{\tau}_{\text{cld}}$ is not large compared to τ_{cld}. At finer resolutions (e.g., $dx = 0.125 - 0.25$ km), however, we have $\kappa < \tau_{\text{cld}}$ and now the modified theory predicts larger anvil cloud fractions for comparable κ, in better agreement with the CRM. The agreement in the mid-troposphere is worse, however, likely because mid-tropospheric clouds at fine resolution do not spread even though the upper-tropospheric anvils do. Finally, at 62.5 m the modified cloud fraction profile in Figure A1 agrees quite well with the CRM, in contrast to the mismatch in Figure 4, but the diagnosed value $\kappa = 1$ min is inconsistent with the value of 18 min found earlier in Figures 4 and 5. The reasons for this mismatch are unclear.

Appendix B: Implications for Relative Humidity

The decrease in PE with resolution seen in the main text has implications for the environmental RH in our simulations, which we explore in this Appendix. Physically, one would expect that the increase in normalized condensate evaporation (Figure 6c) would not only reduce PE, but would also lead to a moister environment and hence increased RH. These expectations may be quantified using the theory of Romps (2014) (hereafter R14), which provided expressions for RH both with and without evaporation, as encapsulated in the parameter $\alpha \equiv e/c$:

$$\mathrm{RH} = \frac{\delta}{\gamma + \delta} \qquad \text{(no evap)} \tag{B1a}$$

$$\mathrm{RH} = \frac{\delta + \alpha\gamma - \alpha\epsilon}{\gamma + \delta - \alpha\epsilon} \quad \text{(with evap)}\ . \tag{B1b}$$

Here δ is the gross fractional detrainment diagnosed from Equation 4, $\gamma \equiv -d\ln q_v^*/dz$ is the "water-vapor lapse rate", and ϵ is the gross fractional entrainment rate diagnosed from the equation $\frac{1}{M}\frac{dM}{dz} = \epsilon - \delta$. Note that $\alpha = e/c$ is also just 1 minus the conversion efficiency shown in Figure 2c, and also that B1b reduces to B1a if $\alpha = 0$. Equation B1a expresses RH in terms of the competing processes of convective moistening (δ) and subsidence drying (γ), while B1b includes the additional effects of detrained condensate evaporation (R14).

Figure B1 shows profiles of RH calculated from Equation B1a and B1b, and as diagnosed directly from the (fixed-grid, warm-rain) simulations. The simulated profiles show that RH increases markedly with horizontal resolution, with mid-tropospheric values ranging from 0.45 at $dx = 16$ km to ~0.9 at $dx = 62$ m. This RH increase is captured by Equation B1b, but is much less consistent with the RH profiles predicted by Equation B1a. This suggests that the PE decreases seen in Figure 7 are largely driving the RH changes seen in Figure B1c, and that the latter are yet another impact of increased evaporation resulting from more efficient mixing at higher resolution. A caveat of these results is that (vertically resolved) rain evaporation should be included in the calculation of α but is currently omitted; comparison with simulations with rain evaporation disabled again shows similar results, however.

It may seem paradoxical that evaporation can increase so markedly with resolution at the same time that RH increases so markedly. Shouldn't a moister environment inhibit evaporation, not promote it? Resolving this requires closer inspection of Equation 8. While indeed increasing RH diminishes the $(1 - \mathrm{RH})$ factor, the $1/dx$ factor (representing mixing timescale) increases strongly with resolution. More quantitatively, mid-tropospheric $(1 - \mathrm{RH})$ decreases from ~0.5 to ~0.1 (a factor of 5) over our resolution range, while $1/dx$ increases by a factor of 256, overwhelming the effects of changing RH.

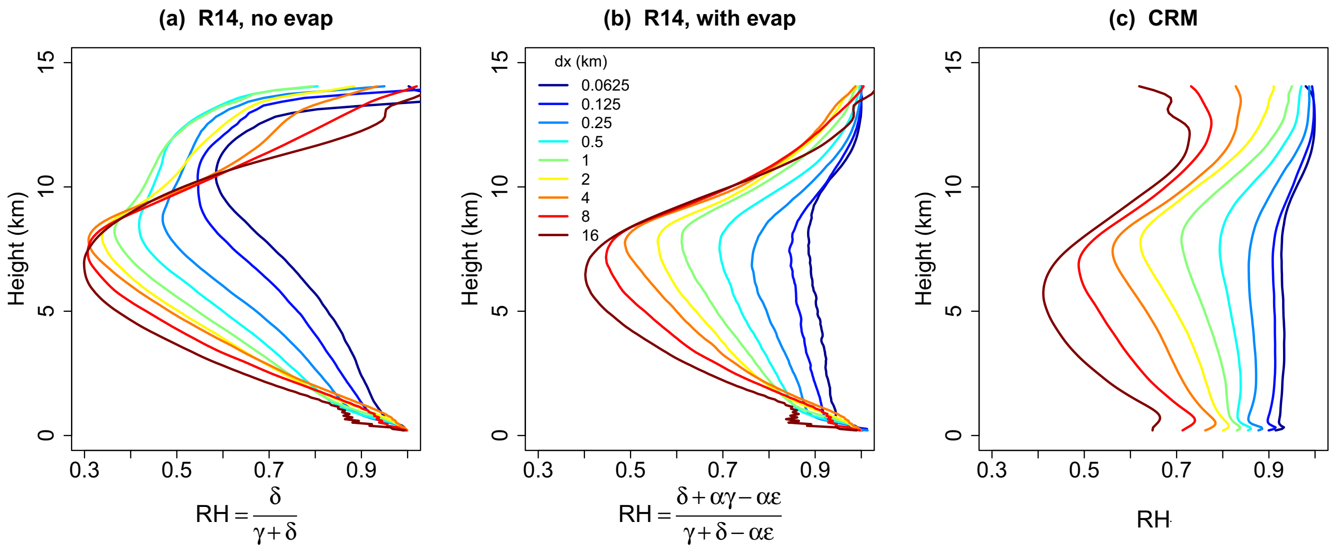

Figure B1. *Relative humidity increases markedly with resolution, driven largely by changes in precipitation efficiency (PE).* These panels show RH profiles at varying resolutions as obtained (a) from Equation B1a, (b) from Equation B1b, (c) directly from the simulations. The simulated RH increases dramatically with resolution (panel c), and this increase is largely reproduced using Equation B1b which includes the effects of PE via the parameter $\alpha = e/c$ (panel b). Omitting PE effects by setting $\alpha = 0$ yields a noticeably worse approximation to the simulated RH profiles (panel a), suggesting that PE changes are a key driver in the resolution sensitivity of RH seen here.

Appendix C: Changes in Clear-Sky Convergence

As discussed in Section 5, our results here seem to conflict with the "clear-sky convergence" (CSC) paradigm for convective detrainment. In this Appendix we review this conflict and reconcile it with our results.

The CSC paradigm may be described as follows (see also S19 and references therein): In steady-state, the clear-sky environment experiences a radiative cooling $\mathcal{H}_{\mathrm{rad}} < 0$ (K/day) which must be balanced by subsidence warming, yielding an environmental subsidence velocity

$$w_{\mathrm{sub}} = \frac{\mathcal{H}_{\mathrm{rad}}}{\Gamma_d - \Gamma} \tag{C1}$$

(Folkins, 2002; Mapes, 1997, 2001, here $\Gamma = -dT/dz$ and $\Gamma_d = g/C_p$ are the actual and dry lapse rates, respectively). The vertical profile of this subsidence velocity will be non-uniform, so that its vertical divergence $\partial_z w_{\mathrm{sub}}$ will be nonzero. This vertical divergence requires equal and opposite convergence in the horizontal, known as clear-sky convergence

$$\mathrm{CSC} = \partial_z \left(\frac{\mathcal{H}_{\mathrm{rad}}}{\Gamma_d - \Gamma} \right) , \tag{C2}$$

which must be sourced from the convecting region and thus equal to (net) convective detrainment. Indeed, profiles of CSC are seen to correspond with those of cloud fraction (Bony et al., 2016; Kuang & Hartmann, 2007; Zelinka & Hartmann, 2010), and a rough equality between net convective detrainment and CSC was shown recently by Beydoun et al. (2021). Thus, net convective detrainment is thought to be governed by the factors appearing in Equation C2, namely radiative cooling $\mathcal{H}_{\mathrm{rad}}$ and moist lapse rates Γ. More specifically, the anvil peak is attributed to a peak in $\partial_z \mathcal{H}_{\mathrm{rad}}$ (Hartmann & Larson, 2002), and changes in anvil cloud area with warming (i.e., the anvil cloud area feedback) have been attributed to moist adiabatic changes in Γ (Bony et al., 2016).

While this CSC paradigm is generally accepted (Hartmann et al., 2019), it lies in clear tension with the results presented here. Our simulations have $\mathcal{H}_{\mathrm{rad}}$ largely fixed by Equation 2 (see Figure C1a below), and naively one would expect the lapse rate Γ in all our simulations to follow the same moist adiabat. This seems to leave little room in Equation C2 for CSC, and hence convective detrainment and cloud fraction, to vary as dramatically as they do in Figures 2d and 1.

The resolution of this paradox is that Equation C1 is missing a potentially large source of environmental cooling, namely condensate evaporation (analysis of simulations with rain evaporation disabled indicate that rain evaporation plays only a minor role). This contributes an evaporative cooling $\mathcal{H}_e = Le/(\rho C_p)$ (all symbols have their usual meaning) which should be added to $\mathcal{H}_{\mathrm{rad}}$ in Equations C1 and C2. Figures C1a and 1b displays profiles of $\mathcal{H}_{\mathrm{rad}}$ and $\mathcal{H}_e$ from our simulations, and shows that while $\mathcal{H}_e$ is small compared to $\mathcal{H}_{\mathrm{rad}}$ at low resolution, it increases by roughly an order of magnitude over our resolution range, and is indeed several times larger than $\mathcal{H}_{\mathrm{rad}}$ at high resolution.

Thus CSC can and should increase with resolution in our simulations, driven by an increase in $\mathcal{H}_e$. This is consistent with (and ultimately equivalent to) the hypothesis 5, which also says that increased evaporation drives increased detrainment. To confirm this we calculate radiative CSC using Equation C2 as written, and also calculate evaporative and total CSC by substituting $\mathcal{H}_e$ and $\mathcal{H}_{\mathrm{rad}} + \mathcal{H}_e$ for $\mathcal{H}_{\mathrm{rad}}$ in Equation C2. These profiles are shown in Figures C1d–C1f, and indeed show that total CSC increases with resolution, due mostly to increases in evaporative CSC.

Interestingly, however, there is also a non-negligible increase in radiative CSC (despite the uniformity of the $\mathcal{H}_{\mathrm{rad}}$ profiles), which can be traced to changes in the upper-tropospheric lapse rate Γ (Figure C1c; mid and lower tropospheric lapse rates are more uniform amongst the simulations and follow a moist adiabat, as expected). These changes in Γ occur just as the troposphere begins to deviate from a moist adiabat and toward the much more stable radiative equilibrium profile of the stratosphere, analogous to the transition to the tropical tropopause layer in the real tropical atmosphere (Fueglistaler et al., 2009). Thus, near the anvil level Γ is unconstrained, yielding another degree of freedom (in addition to $\mathcal{H}_e$) which allows CSC and hence detrainment to vary. Such additional degrees of freedom may complicate simple arguments such as those of Bony et al. (2016), which explains modeled

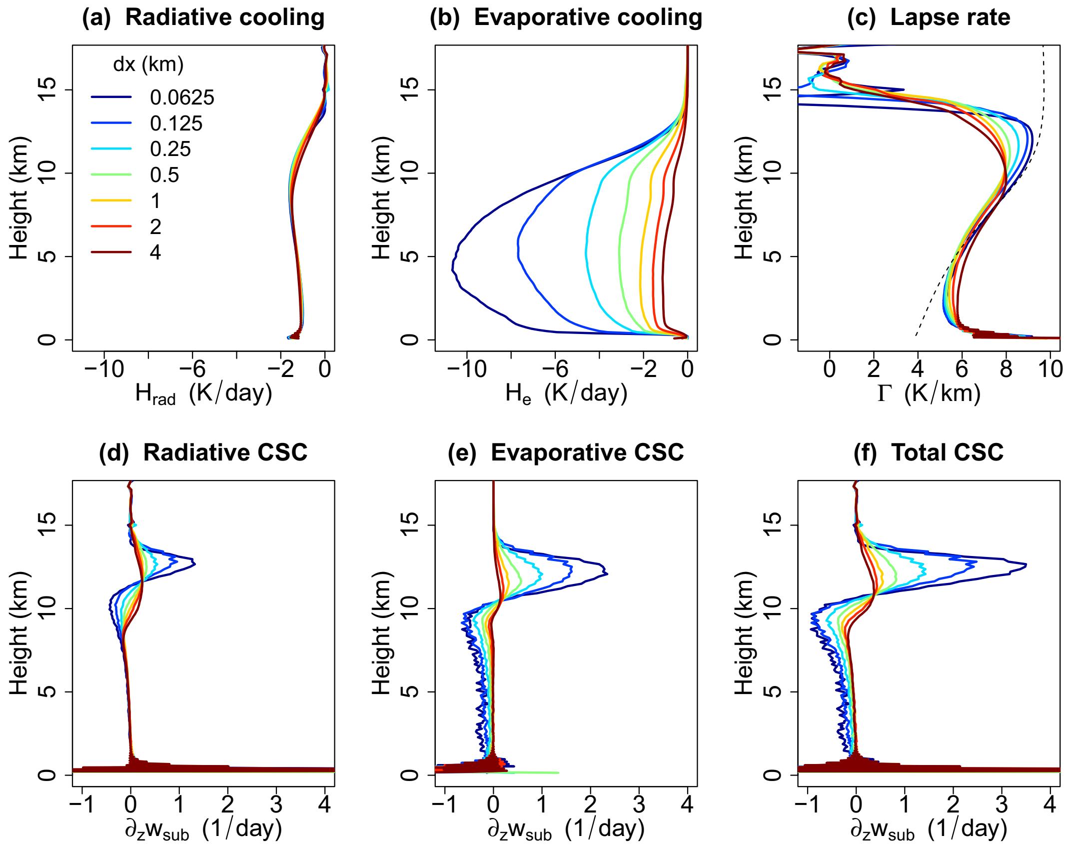

Figure C1. *Clear-sky convergence increases with resolution due largely to evaporation.* Profiles of (a) radiative cooling (b) evaporative cooling (c) lapse rate Γ, diagnosed directly from simulations. Also shown are (d) radiative clear-sky convergence (CSC) (e) evaporative CSC (f) total CSC, as diagnosed from Equation C2 and as discussed in the text. At high resolution evaporative cooling dominates over radiative cooling, as does the corresponding CSC. Changes in radiative CSC stem from changes in upper-tropospheric lapse rate which are unconstrained by the moist adiabat (dashed line in (c), calculated as standard moist pseudo-adiabatic lapse rate using temperature and pressure profiles from the $dx = 0.5$ km simulation). The $dx = 8$, 16 km simulations are omitted in this figure for clarity, as their near-surface air temperatures and corresponding lapse rates differ somewhat from the other simulations.

changes in CSC in terms of the moist adiabatic constraint on Γ. For further caveats and critiques of the CSC paradigm, see S19 and Seeley, Jeevanjee, and Romps (2019).

Data Availability Statement

Data for this project will be available at 10.5281/zenodo.5146193 upon publication.

Acknowledgments
NJ thanks Jake Seeley, Yi Ming, Ming Zhao, Leo Donner, and V. Balaji for discussions and/or comments on early versions of the manuscript. The authors thank three anonymous reviewers for their close reads of this paper and useful feedback.

References

Bauer, P., Stevens, B., & Hazeleger, W. (2021). A digital twin of Earth for the green transition. *Nature Climate Change*, *11*(2), 80–83. https://doi.org/10.1038/s41558-021-00986-y

Beydoun, H., Caldwell, P. M., Hannah, W. M., & Donahue, A. S. (2021). Dissecting anvil cloud response to sea surface warming. *Geophysical Research Letters*, *48*, e2021GL094049. https://doi.org/10.1029/2021GL094049

Bony, S., Stevens, B., Coppin, D., Becker, T., Reed, K. A., Voigt, A., & Medeiros, B. (2016). Thermodynamic control of anvil cloud amount. *Proceedings of the National Academy of Sciences of the USA*, *113*(32), 8927–8932. https://doi.org/10.1073/pnas.1601472113

Brenowitz, N. D., & Bretherton, C. S. (2018). Prognostic validation of a neural network unified physics parameterization. *Geophysical Research Letters*, *45*(12), 6289–6298. https://doi.org/10.1029/2018gl078510

Bryan, G. H., & Morrison, H. (2012). Sensitivity of a simulated squall line to horizontal resolution and parameterization of microphysics. *Monthly Weather Review*, *140*(1), 202–225. https://doi.org/10.1175/MWR-D-11-00046.1

Bryan, G. H., Wyngaard, J. C., & Fritsch, J. M. (2003). Resolution requirements for the simulation of deep moist convection. *Monthly Weather Review*, *131*(10), 2394–2416. https://doi.org/10.1175/1520-0493(2003)131<2394:rrftso>2.0.co;2

Cesana, G., & Chepfer, H. (2012). How well do climate models simulate cloud vertical structure? A comparison between CALIPSO-GOCCP satellite observations and CMIP5 models. *Geophysical Research Letters*, *39*(20). https://doi.org/10.1029/2012GL053153

Chen, J. H., & Lin, S. J. (2013). Seasonal predictions of tropical cyclones using a 25-km-resolution general circulation model. *Journal of Climate*, *26*(2), 380–398. https://doi.org/10.1175/jcli-d-12-00061.1

Cronin, T. W., & Wing, A. A. (2017). Clouds, circulation, and climate sensitivity in a radiative-convective equilibrium channel model. *Journal of Advances in Modeling Earth Systems*, *9*, 2883–2905. https://doi.org/10.1002/2017MS001111

Dawe, J. T., & Austin, P. H. (2010). Interpolation of LES cloud surfaces for use in direct calculations of entrainment and detrainment. *Monthly Weather Review*, *139*(2), 444–456. https://doi.org/10.1175/2010mwr3473.1

De Rooy, W. C., Bechtold, P., Fröhlich, K., Hohenegger, C., Jonker, H., Mironov, D., et al. (2013). Entrainment and detrainment in cumulus convection: An overview. *Quarterly Journal of the Royal Meteorological Society*, *139*(670), 1–19. https://doi.org/10.1002/qj.1959

Folkins, I. (2002). Origin of lapse rate changes in the upper tropical troposphere. *Journal of the Atmospheric Sciences*, *59*(5), 992–1005. https://doi.org/10.1175/1520-0469(2002)059<0992:oolrci>2.0.co;2

Fueglistaler, S., Dessler, A. E., Dunkerton, T. J., Folkins, I., Fu, Q., & Mote, P. W. (2009). Tropical tropopause layer. *Review of Geophysics*, *47*, RG1004. https://doi.org/10.1029/2008RG000267

Harris, L. M., & Lin, S. J. (2013). A two-way nested global-regional dynamical core on the cubed-sphere grid. *Monthly Weather Review*, *141*(1), 283–306. https://doi.org/10.1175/mwr-d-11-00201.1

Hartmann, D. L., Blossey, P. N., & Dygert, B. D. (2019). Convection and climate: What have we learned from simple models and simplified settings? *Current Climate Change Reports*, *5*(3), 196–206. https://doi.org/10.1007/s40641-019-00136-9

Hartmann, D. L., Gasparini, B., Berry, S. E., & Blossey, P. N. (2018). The life cycle and net radiative effect of tropical anvil clouds. *Journal of Advances in Modeling Earth Systems*, *10*(12), 3012–3029. https://doi.org/10.1029/2018MS001484

Hartmann, D. L., & Larson, K. (2002). An important constraint on tropical cloud - Climate feedback. *Geophysical Research Letters*, *29*(20). https://doi.org/10.1029/2002GL015835

Hartmann, D. L., Moy, L. A., & Fu, Q. (2001). Tropical convection and the energy balance at the top of the atmosphere. *Journal of Climate*, *14*(24), 4495–4511. https://doi.org/10.1175/1520-0442(2001)014<4495:tcateb>2.0.co;2

Held, I. M., & Soden, B. J. (2006). Robust responses of the hydrological cycle to global warming. *Journal of Climate*, *19*, 5686–5699. https://doi.org/10.1175/jcli3990.1

Jeevanjee, N. (2017). Vertical velocity in the gray zone. *Journal of Advances in Modeling Earth Systems*, *9*, 2304–2316. https://doi.org/10.1002/2017MS001059

Jeevanjee, N., Hassanzadeh, P., Hill, S., & Sheshadri, A. (2017). A perspective on climate model hierarchies. *Journal of Advances in Modeling Earth Systems*, *9*(4), 1760–1771. https://doi.org/10.1002/2017MS001038

Jeevanjee, N., & Romps, D. M. (2018). Mean precipitation change from a deepening troposphere. *Proceedings of the National Academy of Sciences*, *115*(45), 11465–11470. https://doi.org/10.1073/pnas.1720683115

Kessler, E. (1969). On the distribution and continuity of water substance on atmospheric circulation. *Meteorlogical Monographs*, *10*(32), 1–84. https://doi.org/10.1016/0169-8095(94)00090-Z

Khairoutdinov, M., Randall, D., & DeMott, C. (2005). Simulations of the atmospheric general circulation using a cloud-resolving model as a superparameterization of physical processes. *Journal of the Atmospheric Sciences*, *62*, 2136–2154. https://doi.org/10.1175/JAS3453.1

Kuang, Z., & Hartmann, D. L. (2007). Testing the fixed anvil temperature hypothesis in a cloud-resolving model. *Journal of Climate*, *20*(10), 2051–2057. https://doi.org/10.1175/JCLI4124.1

Langhans, W., Yeo, K., & Romps, D. M. (2015). Lagrangian investigation of the precipitation efficiency of convective clouds. *Journal of the Atmospheric Sciences*, *72*(3), 1045–1062. https://doi.org/10.1175/JAS-D-14-0159.1

Lin, S. J. (2004). A 'vertically Lagrangian' finite-volume dynamical core for global models. *Monthly Weather Review*, *132*(10), 2293–2307. https://doi.org/10.1175/1520-0493(2004)132<2293:avlfdc>2.0.co;2

Lindzen, R. S., Chou, M. D., & Hou, A. Y. (2001). Does the Earth have an adaptive infrared Iris? *Bulletin of the American Meteorological Society*, *82*(3), 417–432. https://doi.org/10.1175/1520-0477(2001)082<0417:dtehaa>2.3.co;2

Lutsko, N. J., & Cronin, T. W. (2018). Increase in precipitation efficiency with surface warming in radiative-convective equilibrium. *Journal of Advances in Modeling Earth Systems*, *10*(11), 2992–3010. https://doi.org/10.1029/2018MS001482

Mapes, B. E. (1997). Mutual adjustment of mass flux and stratification profiles. In *The physics and parameterization of moist atmospheric convection* (pp. 399–411). Springer. https://doi.org/10.1007/978-94-015-8828-7_16

Mapes, B. E. (2001). Water's two scale heights: The moist adiabat and the radiative troposphere. *Quarterly Journal of the Royal Meteorological Society*, *127*, 2353–2366. https://doi.org/10.1002/qj.49712757708

Mauritsen, T., & Stevens, B. (2015). Missing iris effect as a possible cause of muted hydrological change and high climate sensitivity in models. *Nature Geoscience*, *8*(5), 346–351. https://doi.org/10.1038/ngeo2414

Miyakawa, T., & Miura, H. (2019). Resolution dependencies of tropical convection in a global cloud/cloud-system resolving model. *Journal of the Meteorological Society of Japan*, *97*(3), 745–756. https://doi.org/10.2151/jmsj.2019-034

Narenpitak, P., Bretherton, C. S., & Khairoutdinov, M. F. (2017). Cloud and circulation feedbacks in a near-global aquaplanet cloud-resolving model. *Journal of Advances in Modeling Earth Systems*, *9*, 1069–1090. https://doi.org/10.1002/2016MS000872

Ohno, T., Satoh, M., & Noda, A. (2019). Fine vertical resolution radiative-convective equilibrium experiments: Roles of turbulent mixing on the high-cloud response to sea surface temperatures. *Journal of Advances in Modeling Earth Systems*, *11*(6), 1637–1654. https://doi.org/10.1029/2019MS001704

Pauluis, O., & Garner, S. (2006). Sensitivity of radiative convective equilibrium simulations to horizontal resolution. *Journal of the Atmospheric Sciences*, *63*(7), 1910–1923. https://doi.org/10.1175/JAS3705.1

Prein, A. F. (2015). A review on regional convection-permitting climate modeling: Demonstrations, prospects, and challenges. *Reviews of Geophysics*, *53*, 323–361. https://doi.org/10.1002/2014RG000475

Rasp, S., Pritchard, M. S., & Gentine, P. (2018). Deep learning to represent subgrid processes in climate models. *Proceedings of the National Academy of Sciences of the USA*, *115*(39), 9684–9689. https://doi.org/10.1073/pnas.1810286115

Roh, W., Satoh, M., & Hohenegger, C. (2021). Intercomparison of cloud properties in DYAMOND simulations over the atlantic ocean. *Journal of the Meteorological Society of Japan. Ser. II*, *99*, 1439–1451. https://doi.org/10.2151/jmsj.2021-070

Romps, D. M. (2008). The dry-entropy budget of a moist atmosphere. *Journal of the Atmospheric Sciences*, *65*(12), 3779–3799. https://doi.org/10.1175/2008JAS2679.1

Romps, D. M. (2010). A direct measure of entrainment. *Journal of the Atmospheric Sciences*, *67*(6), 1908–1927. https://doi.org/10.1175/2010JAS3371.1

Romps, D. M. (2014). An analytical model for tropical relative humidity. *Journal of Climate*, *27*(19), 7432–7449. https://doi.org/10.1175/JCLI-D-14-00255.1

Romps, D. M. (2020). Climate sensitivity and the direct effect of carbon dioxide in a limited-area cloud-resolving model. *Journal of Climate*, *33*(9), 3413–3429. https://doi.org/10.1175/jcli-d-19-0682.1

Satoh, M., Stevens, B., Judt, F., Khairoutdinov, M., Lin, S. J., Putman, W. M., & Düben, P. (2019). Global cloud-resolving models. *Current Climate Change Reports*, *5*, 172–184. https://doi.org/10.1007/s40641-019-00131-0

Seeley, J. T., Jeevanjee, N., Langhans, W., & Romps, D. M. (2019). Formation of tropical anvil clouds by slow evaporation. *Geophysical Research Letters*, *46*(1), 492–501. https://doi.org/10.1029/2018GL080747

Seeley, J. T., Jeevanjee, N., & Romps, D. M. (2019). FAT or FiTT: Are anvil clouds or the tropopause temperature invariant? *Geophysical Research Letters*, *46*(3), 1842–1850. https://doi.org/10.1029/2018GL080096

Sherwood, S. C., Webb, M. J., Annan, J. D., Armour, K. C., Forster, P. M., Hargreaves, J. C., et al. (2020). An assessment of Earth's climate sensitivity using multiple lines of evidence. *Reviews of Geophysics*, *58*(4), e2019RG000678. https://doi.org/10.1029/2019rg000678

Singh, M. S., & O'Gorman, P. A. (2015). Increases in moist-convective updraught velocities with warming in radiative-convective equilibrium. *Quarterly Journal of the Royal Meteorological Society*, *141*(692), 2828–2838. https://doi.org/10.1002/qj.2567

Stevens, B., Satoh, M., Auger, L., Biercamp, J., Bretherton, C. S., Chen, X., et al. (2019). Dyamond: The DYnamics of the atmospheric general circulation modeled on non-hydrostatic domains. *Progress in Earth and Planetary Science*, *6*(1). https://doi.org/10.1186/s40645-019-0304-z

Su, H., Jiang, J. H., Zhai, C., Perun, V. S., Shen, J. T., Del Genio, A., et al. (2013). Diagnosis of regime-dependent cloud simulation errors in CMIP5 models using a-Train satellite observations and reanalysis data. *Journal of Geophysical Research: Atmospheres*, *118*(7), 2762–2780. https://doi.org/10.1029/2012jd018575

Sui, C. H., Satoh, M., & Suzuki, K. (2020). Precipitation efficiency and its role in cloud-radiative feedbacks to climate variability. *Journal of the Meteorological Society of Japan*, *98*(2), 261–282. https://doi.org/10.2151/jmsj.2020-024

Tsushima, Y., Iga, S. I., Tomita, H., Satoh, M., Noda, A. T., & Webb, M. J. (2014). High cloud increase in a perturbed SST experiment with a global nonhydrostatic model including explicit convective processes. *Journal of Advances in Modeling Earth Systems*, *6*(3), 571–585. https://doi.org/10.1002/2013MS000301

Voosen, P. (2020). Europe is building a 'digital twin' of Earth to revolutionize climate forecasts. *Science*. https://doi.org/10.1126/science.abf0687

Williams, I. N., & Pierrehumbert, R. T. (2017). Observational evidence against strongly stabilizing tropical cloud feedbacks. *Geophysical Research Letters*, *44*(3), 1503–1510. https://doi.org/10.1002/2016gl072202

Wing, A. A., Stauffer, C. L., Becker, T., Reed, K. A., Ahn, M., Arnold, N. P., et al. (2020). Clouds and convective self-aggregation in a multi-model ensemble of radiative-convective equilibrium simulations. *Journal of Advances in Modeling Earth Systems*, *12*(9), e2020MS002138. https://doi.org/10.1029/2020ms002138

Yuval, J., & O'Gorman, P. A. (2020). Stable machine-learning parameterization of subgrid processes for climate modeling at a range of resolutions. *Nature Communications*, *11*(1), 3295. https://doi.org/10.1038/s41467-020-17142-3

Zelinka, M. D., & Hartmann, D. L. (2010). Why is longwave cloud feedback positive? *Journal of Geophysical Research*, *115*(D16), D16117. https://doi.org/10.1029/2010JD013817

Zelinka, M. D., Zhou, C., & Klein, S. A. (2016). Insights from a refined decomposition of cloud feedbacks. *Geophysical Research Letters*, *43*(17), 9259–9269. https://doi.org/10.1002/2016gl069917

Zhou, L., Lin, S. J., Chen, J. H., Harris, L. M., Chen, X., & Rees, S. L. (2019). Toward convective-scale prediction within the next generation global prediction system. *Bulletin of the American Meteorological Society*, *100*(7), 1225–1243. https://doi.org/10.1175/BAMS-D-17-0246.1